GNC 2014: 9th International ESA Conference on Guidance, Navigation & Control Systems
Porto, Portugal | 2 - 6 June 2014
European Space Agency

BREADBOARD MODEL OF A 3D LIDAR SENSOR FOR REAL-TIME POSE ESTIMATION OF SPACECRAFT

F. Rems[1], S. Fritz, T. Boge[2].
German Aerospace Center (DLR), Münchener Straße 20, 82234 Weßling, Germany,
[1]florian.rems@dlr.de, [2]toralf.boge@dlr.de.

ABSTRACT

Reliable relative navigation between two spacecraft is a critical element of future On Orbit Servicing (OOS) missions and space debris removal scenarios. Sensors are required that allow for accurate estimates of a target satellite's relative position and attitude. Scanning LiDAR (Light RADAR, also Light Detection And Ranging) based sensors are capable of creating a three dimensional point cloud of the target satellite, widely immune to varying illumination conditions. In this context, a 3D LiDAR sensor for real-time tracking and pose estimation of a target satellite is developed at the German Space Operations Center (GSOC), part of the German Aerospace Center (DLR). It is intended as an on-ground research platform for development and test of LiDAR related algorithms and concepts.

The sensor is based on a commercial 2D laser scanner which is extended by an additional high precision rotary axis. An integral part of the hardware is a smart adjustment mechanism allowing precise mechanical calibration of the sensor, thereby optimizing the coverage by the scanning pattern and simplifying the necessary software models for measurement evaluation considerably. Scanner and axis are synchronized by continuous high frequency sampling of the axis angle. For controlling the sensor and for real-time pre-processing of the raw range data an embedded system is used. First tests were conducted in a robotic Rendezvous and Docking laboratory (European Proximity Operations Simulator - EPOS), involving realistic illumination conditions.

This paper outlines hardware design, sensor control and processing architecture of the LiDAR sensor breadboard. Results of first tests, including accuracy and sensitivity to illumination, are presented and discussed.

1. INTRODUCTION

Autonomous spacecraft relative navigation is a key technology for many future space mission concepts. In On-Orbit Servicing (OOS) scenarios a servicing satellite approaches a client/target satellite and performs maintenance tasks to prolong the client satellite's lifetime [1, 2, 3]. Active Space Debris Removal (ADR) represents a similar scenario, save for its purpose: instead of maintaining a client spacecraft, a defective satellite or some space debris object shall be deorbited in a controlled fashion thus eliminating the danger of collision for other satellites [4, 5].

The approach, especially the last phase at close range, constitutes a critical element in these mission scenarios. Since position and orientation, i.e. the pose of the target are unknown in most cases, the servicing spacecraft has to be equipped with appropriate sensors and processing capability to obtain information about the relative pose of the target. This is the basis upon which the servicer's autonomous GNC system carries out approach and - in some scenarios - capture of the target.

Among the different types of sensors that are used for spacecraft relative navigation are scanning LiDARs (Light RADAR, also Light Detection and Ranging). A LiDAR determines the range to some surface by emitting a laser beam and by analyzing the backscattered light. A three-dimensional point cloud is generated by using some kind of mirror system for deflecting the laser beam periodically. In contrast to conventional cameras, LiDAR sensors provide real range information directly. The greatest advantage of scanning LiDAR sensors is high immunity to dynamic illumination conditions due to the very small instantaneous Field of View (FOV). There are a few LiDAR sensor systems that have illustrated the suitability of scanning LiDAR technology for spacecraft relative navigation. Among these: The Spaceborne Scanning LiDAR System (SSLS) was part of the Air Force Research Laboratory's space technology demonstration mission XSS-11, launched in 2005 [6]. The Rendezvous Sensor Telegoniometer (RVS-TGM), developed by Jena Optronik GmbH, is an integral part of ESA's Automated Transfer Vehicle (ATV) [7]. The TriDAR, a hybrid scanner combining LiDAR and triangulation technology that has been developed by Neptec Design Group Ltd., was tested successfully as Detailed Test Objective (DTO) on STS-128, STS-131 and STS-135 [8].

At the German Space Operations Center (GSOC), part of the German Aerospace Center (DLR), research is conducted in the field of automated Rendezvous and Docking (RvD). In particular, the On-Orbit Servicing &

Autonomy group works on vision based autonomous relative navigation. In this context, image processing algorithms and GNC software are developed and tested in Hardware-in-the-Loop simulations [9] involving the robotics-based European Proximity Operations Simulator (EPOS) [10]. Conventional visual navigation using a CCD camera is evaluated [11, 12]. But also a more recent technology, the Photonic Mixer Device (PMD) which is a time of flight camera, is applied [13].

To supplement this repertoire of sensors for spacecraft relative navigation, a scanning LiDAR is being developed by GSOC's On-Orbit-Servicing & Autonomy group. We do not intend to build a system to be applied in a real space mission. Rather, the sensor's *primary purpose* is to provide three-dimensional LiDAR data in real-time for research and development of GNC software and algorithms and associated HiL tests at EPOS. The sensor shall be comparable in performance to the aforementioned spaceborne LiDAR systems [6,7,8], yet only within a required range of 25 m. In particular, the range accuracy shall be better than 50 mm and the angular accuracy better than 0.1°. The sensor's *secondary purpose* is to serve as a research platform for novel concepts and algorithms for scanning LiDAR technology in the context of spacecraft relative navigation. The LiDAR shall be based on Commercial of the Shelf (COTS) components as far as possible to keep the development effort at a minimum.

The objective of this paper is to describe the LiDAR sensor hardware, that is to say the Sensor Head, to give an overview about control and processing architecture and to present preliminary test results obtained at EPOS.

2. SENSOR HEAD

The right side of Fig.1 shows a photo of the completely assembled Sensor Head. At the left side, a CAD drawing (housings and cabling removed) illustrates the principle components of the Sensor Head. A 2D LiDAR scanner is mounted on an adjustment mechanism. A servo with integrated controller drives the sensor. A rotary encoder measures the axis angle. And a slip ring transports power and data.

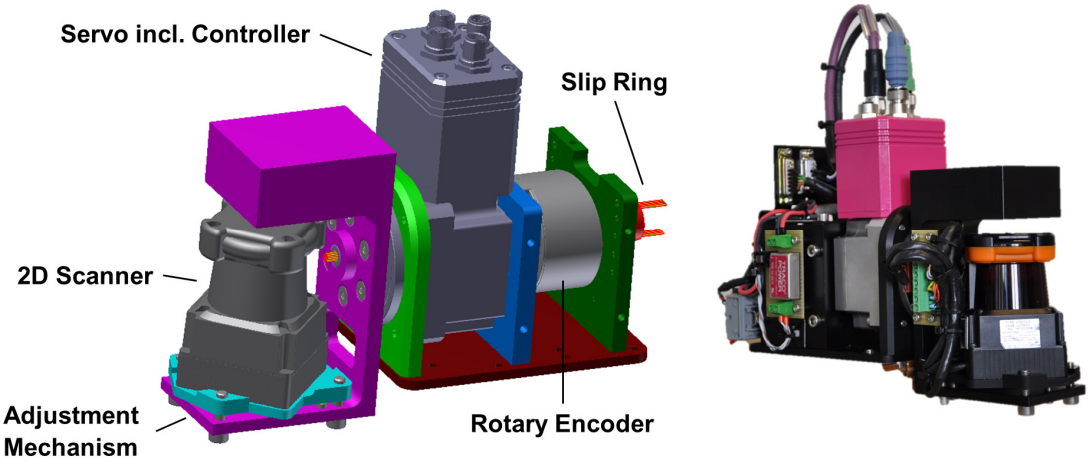

Fig. 1: *Overview of Sensor Head. Left: CAD drawing with housing and cabling removed. Right: Photo of the completely assembled Sensor Head.*

In the following, we will assemble the Sensor Head step by step, thereby illustrating the motivation and requirements behind the individual design choices.

A. BASIS: HOKUYO 2D LASER RANGEFINDER

The basis of the sensor is the commercial Hokuyo UTM-30LX 2D laser rangefinder. It uses an eye-safe laser with a wavelength of 905 nm to scan circumferentially about axis A in a two-dimensional plane, see Fig.2. It measures the distance to obstacles at a maximum range of 30 m as well as the amplitude of the backscattered light. The angular resolution is 0.25°. One "line scan" takes 25 ms. The 2D scanner has a large beam divergence of 0.1° x 0.8° (according to manufacturer). This will undoubtedly also restrict the maximum range at which point cloud measurements of the target object can be obtained with reasonable quality. At the present time, the precise practical impact of this beam divergence on pose estimation efforts within the sensor's range is yet to be

evaluated. Note that the scan plane spans 270°; there is a blind range of 90° as depicted in Fig.2. In [14] a detailed specification of the 2D scanner can be found. Henceforth, the Hokuyo UTM-30LX 2D laser rangefinder will be denoted UTM-30LX in this paper.

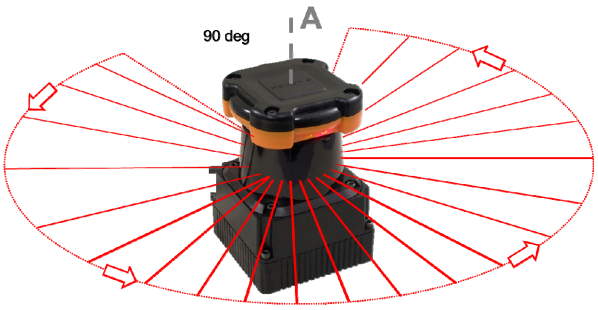

Fig. 2: *Hokuyo UTM-30LX 2D laser scanner with circumferential scan plane. (Photo source: http://de.manu-systems.com/images/L/UTM-30LX.jpg, modified)*

B. SCANNING PATTERNS

How to use the two-dimensional scan plane of the UTM-30LX to generate a three-dimensional point cloud? We consider two possibilities:

By having the scan plane nod up and down around an additional axis that rotates the UTM-30LX - henceforth called axis B - a nodding pattern can be obtained, see the left part of Fig.3. B is oriented perpendicularly to the Region of Interest (ROI), i.e. the expected direction of the target. The resulting pattern resembles a raster scan, somewhat similar to a traditional camera image.

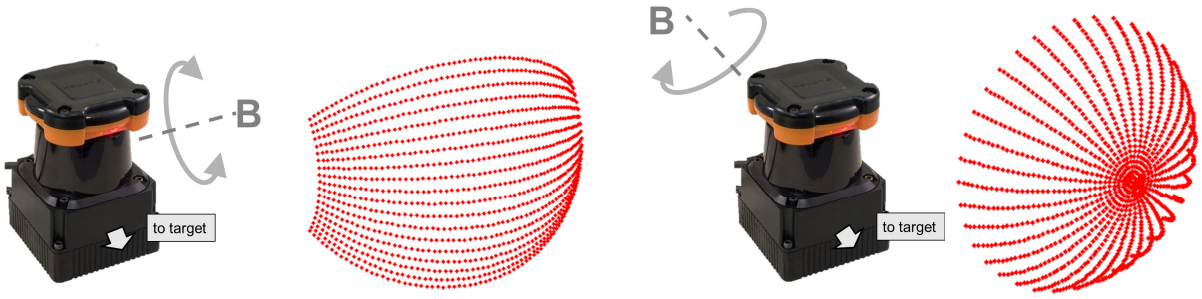

Fig. 3: *Left: Nodding pattern. Right: Centric pattern. (Note: Deformation of the scan lines due to continuously rotating scanner neglected, consistent with a very small rotational speed around axis B.)*

By having the scan plane roll continuously around axis B, a centric pattern can be obtained, see the right part of Fig.3. B is oriented towards the ROI, i.e. the expected direction of the target.

While the nodding pattern allows focusing the scan lines on the target object by adjusting amplitude and center of axis B oscillation, the areas of largest point density are located perpendicularly to the target, far away from the ROI. Furthermore, the continuous rotary acceleration of the UTM-30LX around B leads to a relatively large power demand. The centric pattern concentrates the area of largest point density on the ROI where the target is expected to be and can be realized by continuous rotation of B leading to a lower power demand. However, there is no possibility of focusing the scan lines on the target and the continuous rotation results in a higher constructive effort. See also [15] for an analysis of different scanner configurations.

Considering the secondary purpose of the sensor, it shall be able to realize both the nodding and the centric pattern. Any mechanical modification of the hardware when changing from one pattern to another shall be avoided. This is achieved by a concept depicted in Fig.4. The configuration is switched between nodding and centric pattern by simply turning the complete Sensor Head through 90° with respect to the Region of Interest.

Moreover, the UTM-30LX is mounted at an angle of 45° in the rotor frame to position the blind scan range (90°) such that the effective Field of View (FoV) in both configurations is maximized.

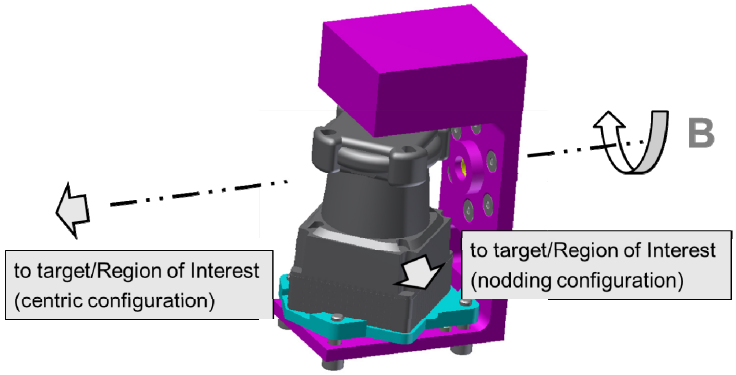

Fig. 4: *UTM-30LX mounted in rotor frame. Nodding and centric pattern are realized by orienting the whole LiDAR sensor appropriately with respect to the Region of Interest.*

The centric pattern offers the interesting possibility of rotating the UTM-30LX continuously. For that purpose, power and data connections of the UTM-30LX have to be designed for limitless rotary transfer. This is realized by a standard slip-ring manufactured by LTN Servotechnik GmbH [16]. Note in Fig.5 that the cabling is placed in a hollow shaft on which the servo and the encoder – both also provided with hollow shafts - are mounted. This results in a very compact design despite the need for rotary energy and power transmission.

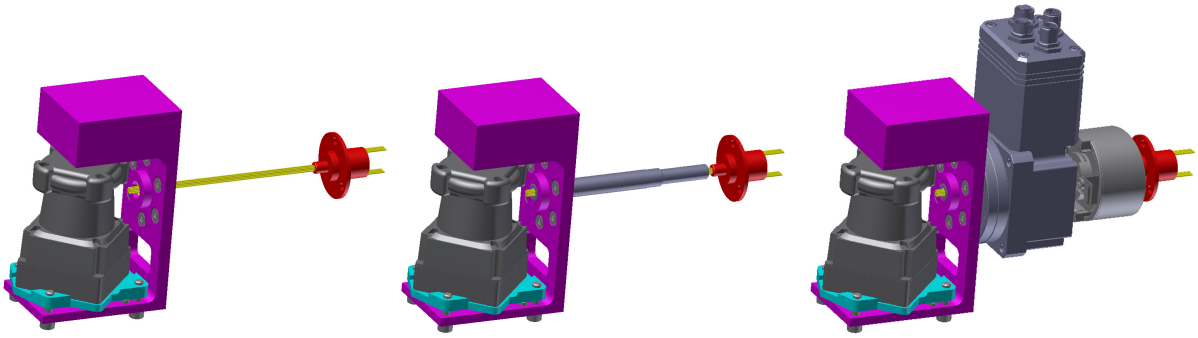

Fig. 5*: Cabling (yellow) in hollow shaft connected to slip-ring (red), servo (dark grey), encoder (light grey).*

C. MECHANICAL CALIBRATION

Ideally, axis A and axis B intersect perpendicularly such that B lies in the scan plane. In the centric configuration, this results in a pattern as already depicted in Fig.3 and also in the left part of Fig.6. However, this ideal orientation may not be achieved in practice due to assembly and component tolerances. For example, according to the manufacturer the UTM-30LX' axis A has an assembly tolerance of ±0.5° with respect to the base plate. So, in general, there will be a small misalignment between the scan plane and axis B, as illustrated in the right part of Fig.6. As a consequence, a blind spot around axis B – near the rough direction of the target object - has to be expected. This spot is located precisely where the centric pattern is supposed to generate the highest point density, obliterating this advantage. All other deviations from the ideal mounting can either be neglected (expected translational deviations of few mm) or be eliminated by software calibration (angular deviations around A or B).

The angular misalignment between B and the scan plane has to be eliminated mechanically by using an adjustable mounting for the UTM-30LX. Since this mounting is rotated along with the UTM-30LX around B, it should have a low mass/inertia. However, at the same time, the adjustable mounting has to be as stiff as possible to avoid any additional dynamic effects on measurement accuracy.

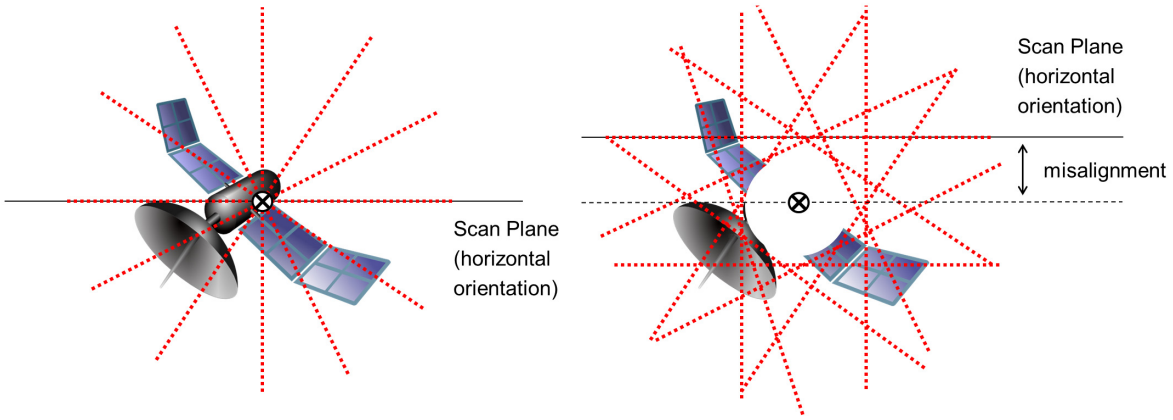

***Fig. 6**: Effect of scan plane misalignment.*

Fig.7 illustrates the solution. The UTM-30LX is fixed to an additional plate (cyan) which is mounted on the rotor frame (magenta). Three pressure screws unambiguously define the distance between the plate and the rotor at three distinct points. By adjusting these screws individually or in combination the UTM-30LX can be tilted in any direction. Especially the misalignment explained above can be compensated. Also, translational errors along axis A can be eliminated. The advantage of this solution is its simplicity and consequent compactness, low mass and high stiffness. However, this is payed for with a tedious and iterative calibration procedure; the pressure screws are kinematically coupled so that in general multiple screws have to be adjusted in order to tilt or shift the UTM-30LX in a certain direction.

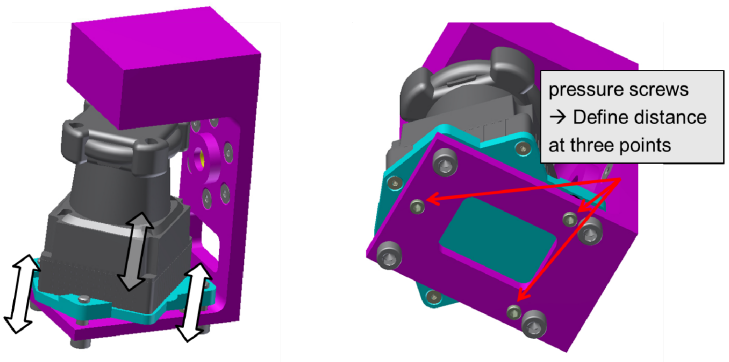

***Fig. 7**: Adjustable mounting.*

For the mechanical calibration, we follow a simple yet effective strategy. Here, we merely outline the basic principle since the detailed procedure is out of the scope of this paper. The strategy is based on analyzing measurements in relative relation to one another, without the need for any absolutely gauged reference object. The basic idea: The scanner is directed towards some plane which has to be inclined with respect to axis B. One line scan is measured. The rotor is turned through an angle of 180° and an additional line scan is taken. Considering that one point of the first line scan corresponds to the very point of the second line scan deflected at the central laser beam (180° turn), both line scans should coincide if axis B lies in the scan plane. Otherwise there should be a difference. This difference is iteratively reduced by executing the procedure multiple times and adjusting the pressure screws accordingly at each iteration. We carried out this manual procedure until the maximum difference between the turned line scan pairs was in the order of magnitude of the UTM-30LX's standard deviation (compare "no illumination" in Fig.13).

D. AXES SYNCHRONISATION

The overall precision of the LiDAR sensor strongly depends on the measurement precision of the instantaneous angle of axis B, henceforth denoted β. To determine that angle, a high precision absolute rotary encoder manufactured by Sick AG is used. It is mounted on the hollow shaft as illustrated in Fig.5. The encoder measures the angular displacement between its outer housing and its inner (also hollow) shaft. The use of an

absolute encoder (in contrast to an incremental encoder) obliterates the need for an additional sensor to define a reference angle. The encoder's resolution is 18 bits, making 262144 steps or about 0.0014°, with an accuracy of ±0.03°. [17]

In general, each scan point must be related to the very value of β (continuously provided by the encoder) at the very time when this point is measured. This synchronization is no trivial task. The UTM-30LX doesn't output point after point in real-time. Rather, a complete scan line, including a timestamp, is provided after each revolution of axis A via USB interface. Fortunately, the UTM-30LX additionally triggers a synchronization impulse using a dedicated binary output, at a specific angle of axis A each revolution. We can assume that the rotational speed of axis A is constant. Given these boundary conditions, we choose a strategy as depicted in Fig.8.

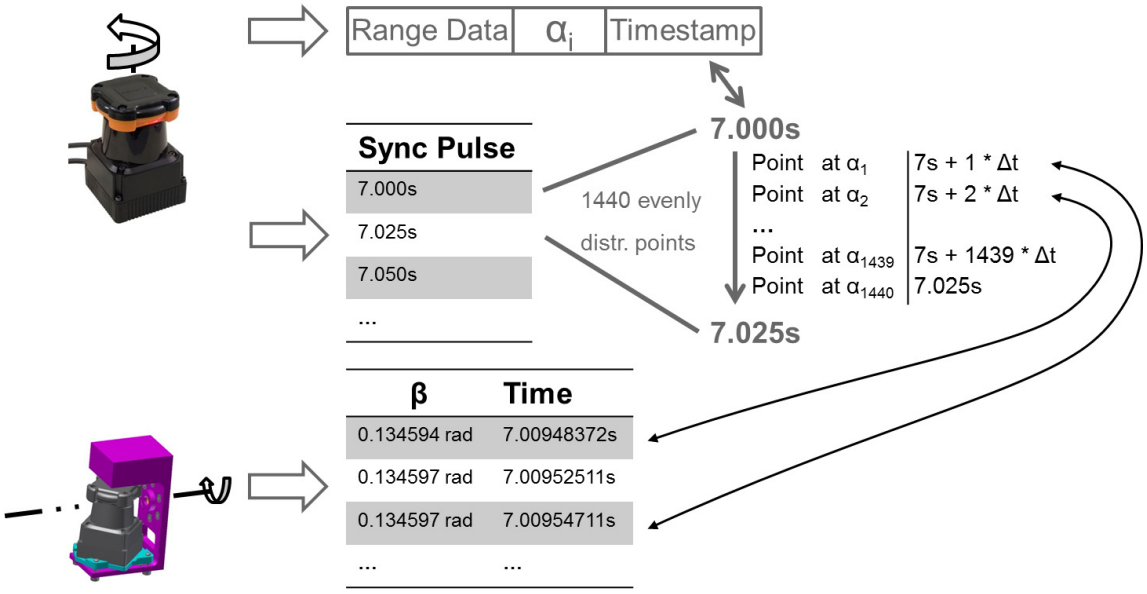

***Fig. 8**: Synchronization strategy.*

The range data is provided by the UTM-30LX. This data is comprised of a list of scan points including implicitly the according angles α of axis A and a single timestamp for a complete line scan, i.e. for precisely one revolution of axis A. The exact time the UTM-30LX periodically fires the sync pulse (once per revolution of axis A) is logged continuously. Implicitly, this records the value of α over time. Utilizing the high resolution absolute encoder, the angle β of axis B is sampled and logged along with the according time. The scan points are distributed evenly over angle α and they are measured at the same values of α at each revolution. If we now assume that axis A rotates with constant velocity, the sync pulses alone are sufficient to relate every scan point to a specific point in time (in-between two sync pulses). This point in time can now be correlated with the list of axis B angles to obtain the value of β for the individual scan point. Finally, the range data packet is related to a sync pulse interval using the data packet timestamp.

The accuracy of this approach depends on

a) the angular accuracy of the UTM-30LX,
b) the accuracy of the encoder,
c) the quality of a common time reference for the internal clock of the UTM-30LX (timestamp in the range data packet provided via USB) and the clock used to log sync pulses and β,
d) the accuracy of sync pulse logging,
e) the assumption that axis A rotates at constant speed and
f) the sampling rate of angle β.

UTM-30LX and encoder have been chosen to meet – among other constraints – points a) and b). c) and d) can be expected to be manageable with standard hardware. However, concerning e), the stability of A's rotational speed is to be evaluated in practice. In general, too large accelerations of the UTM-30LX are to be avoided to not impose undesirable torque on axis A. f) can be handled by sampling β at a sufficiently high frequency. If this frequency is low, then the gaps between the individual samples of β are large and an error caused by

relating a specific point of a sync pulse interval with the timely nearest sample of β is introduced. Interpolation can diminish the problem. But still a high sample frequency is the preferred method for decreasing the error. The error's impact on measurement accuracy of the sensor system has also to be determined in practice.

At the time this paper is written, implementation of this synchronization strategy is ongoing.

E. DRIVING THE SCANNER

Axis B of the LiDAR sensor is motored by a highly integrated servo – a CobraDrive 14C-30-ECC manufactured by Harmonic Drive AG. It is depicted in Fig.5 (right) in dark grey. This servo combines a motor with a playfree gear and a servo controller which has a CAN interface (Controller Area Network). The high level functionality of this controller simplifies commanding the servo considerably. See [18] for more details about the CobraDrive servo.

Note that the mounting frame of the Hokuyo scanner is fixed directly to the flange of the servo. The hollow shaft the encoder is mounted to goes through the hollow shaft of the CobraDrive without touching it and has only to transmit a minimum torque to drive the encoder and the slip ring. This results in a stiff connection of scanner rotor and encoder, minimizing measurement errors due to skewing of the shaft.

3. SENSOR CONTROL AND PROCESSING ARCHITECTURE

This section is intended to give an overview of the sensor system architecture as it is planned. Similarly to the synchronization strategy, implementation is ongoing at the time this paper is written.

A number of requirements have to be taken into account designing the sensor control and processing architecture. The components have to be combined to a system providing 3D point clouds of the target intermediately and completed pose estimates eventually. The major tasks involved are

- interfacing with all sensor components,
- coordinated control of all sensor components,
- realization of the axes synchronization strategy,
- processing of the point cloud (filtering, pose estimation) and
- communication with a host.

Axes synchronization demands sampling and logging of sync pulses and axis B angles at a high frame-rate in real-time. This can be realized very elegantly with a Field Programmable Gate Array (FPGA). Other tasks, like communication with a host and general coordinated control of UTM-30LX and servo are not well suited for FPGA implementation and are better realized conventionally in software.

Before this background, we have chosen to combine the advantages of an FPGA and a conventional CPU. A high level overview is depicted in Fig.9. On the left side, the principal components of the Sensor Head (SH) are depicted. Interfacing with these components, the Control And Processing Unit (CAPU) is shown on the right side. This system is separated into an FPGA part and a CPU part, both parts working together and being strongly coupled. In the following, we describe the CAPU's subsystems.

The Sensor Controller (SC) is a superordinate component which coordinates the other parts of the system and communicates with a host via Ethernet.

The Scan Engine (SE) commands the servo (CAN – Controller Area Network) and interfaces with the UTM-30LX (USB) for commanding and receiving the range data. Moreover, the Scan Engine is connected to the Sync IP-Core (IP – Intellectual Property), implemented on the FPGA, which is supplied with the sync pulse of the UTM-30LX as well as with the current angle of axis B by the encoder (SSI – Synchronous Serial Interface). In terms of the synchronization strategy, the Sync IP-Core accurately logs the sync pulses and samples β continuously. It also relates the timely and angularly evenly distributed scan points within a sync pulse interval with the sampled values of β. In this way, the Scan Engine is supplied with a list of values of β for each sync pulse interval. The Scan Engine relates a range data packet, which includes a timestamp, with the corresponding sync pulse interval and, by using the list of β values, eventually obtains for each scan point: range, α, β and time. Another task of the Scan Engine is to realize a certain scanning pattern by commanding the CobraDrive servo and the UTM-30LX in a coordinated fashion.

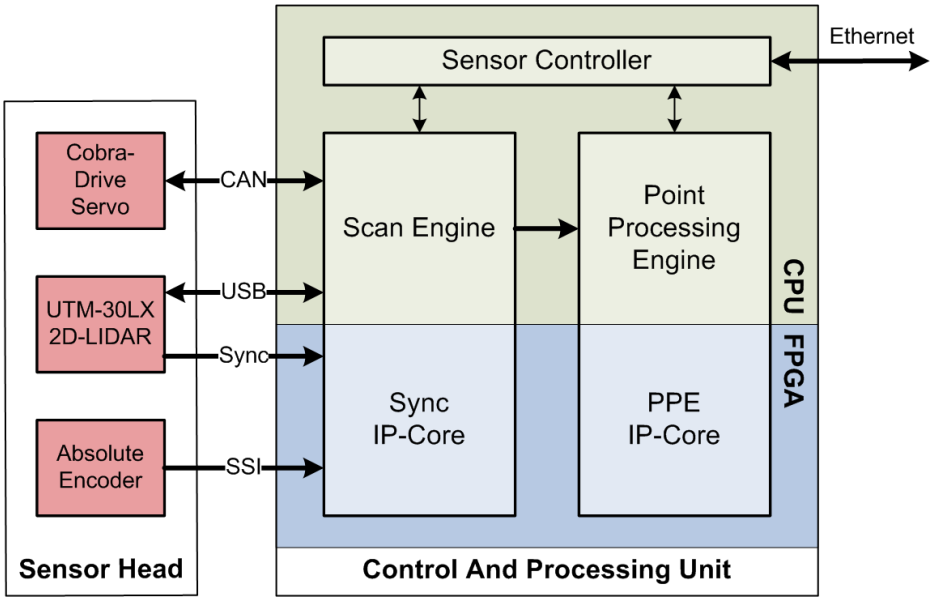

***Fig. 9**: High level sensor system architecture.*

The Point Processing Engine (PPE) handles the point cloud provided by the Scan Engine. This incorporates filtering of the point cloud to identify invalid points, pose initialization and subsequent continuous pose estimation of the target object. In a first stage, these functions are implemented exclusively on the CPU part with a consequent relatively low execution speed. In a second stage, a PPE IP-Core is implemented on the FPGA part that executes simple but computationally expensive calculations required for the filtering, pose initialization and pose estimation algorithms. The PPE IP-Core can be considered a highly specialized co-processor for the Point Processing Engine.

We have chosen the Altera Cyclone V SoC Development Board for implementing this sensor control system. Its core is a Cyclone V SoC which combines an ARM Cortex A9 dual-core CPU and an Altera FPGA on a single chip. This guarantees easy and high performance interfacing between CPU and FPGA part which is beneficial, if not required, for the sensor system architecture illustrated above. Furthermore, the development board already provides all needed interfaces: Ethernet for communicating with a host, USB for connecting to the UTM-30LX, GPIO for sync pulse sampling and realization of the SSI interface, CAN for controlling the servo. [19]

4. PRELIMINARY TESTS AND RESULTS

In the following, we present some first test point clouds generated by the LiDAR sensor. Since the implementation of the sensor control system – outlined in the last section – is still in progress, the point clouds were generated manually. UTM-30LX and CobraDrive servo were connected to a PC and controlled by using standard tools provided by the manufacturers. Line after line was scanned and saved manually. In-between the servo was turned through a specified angular range. After the measurements had been taken, the individual scan lines were assembled manually in MATLAB for analysis and visualization.

It should be noted here that for these preliminary tests at this stage of development the sensor was not calibrated. The purpose of the tests was to demonstrate that the Sensor Head is, in principle, capable of generating a three-dimensional point cloud of a target object and to get a first idea about the influence of realistic illumination conditions with respect to the space environment.

The tests were conducted at GSOC's European Proximity Operations Simulator (EPOS). Fig.10 gives an overview of the laboratory. Two standard industrial robots – one of them mounted on a linear real – constitute the main elements of the facility. Each robot has six Degrees of Freedom (DOF). Along with one DOF of the linear rail, 13 DOF are available for simulating the relative position and orientation of two spacecraft in Rendezvous and Docking (RvD) scenarios. A real-time control system allows conducting Hardware-in-the-Loop (HiL) tests with real sensors and true-to-scale satellite mockups. A 12 kW daylight spotlight provides realistic illumination conditions concerning power density and sun-resembling spectrum. [10]

Fig. 10: *Left: Look into the EPOS laboratory with exemplary satellite mockups. Right: Layout of the EPOS facility.*

The test setup in the EPOS laboratory is depicted in Fig.11. The LiDAR sensor is mounted to the robot at the left. (Additionally mounted components stem from other experiments and have nothing to do with the LiDAR tests.) On the right, a simple satellite mockup is mounted to the robot on the linear rail. At the center, the satellite mockup has a circular indentation, which we expect the sensor to depict clearly. Also, the 12 kW daylight spotlight is used for these tests.

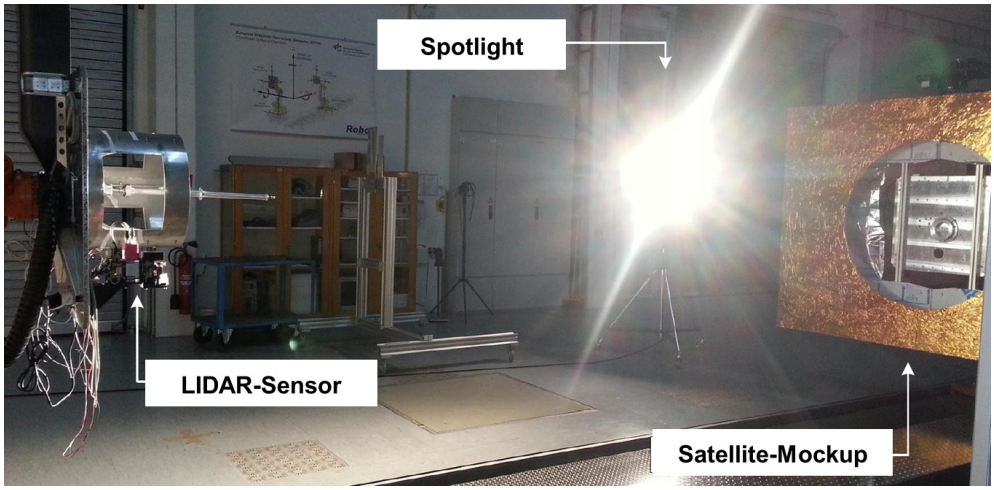

Fig. 11: *Test setup in the EPOS laboratory.*

For these preliminary tests, the relative position and orientation of sensor and satellite mockup was kept constant during the measurements. Fig.12 shows the resulting point clouds. At the left side, we have used the nodding configuration with a step size of 1° for axis B. At the right side the centric configuration is depicted with a step size of 5°. At the upper part of the figure, the point cloud is seen from the perspective of the sensor and at the lower part it is shown from top.

The circular indentation of the mockup can be seen distinctly, especially if looked at from top. The nodding pattern results in a raster scan with a uniform point distribution. In contrast, the centric pattern leads to a high point density at the center of the point cloud exactly in the area where we expect the target satellite to be (at close range approach). However, the centric configuration test required half a rotation around axis B, while the nodding configuration test only required a rotation through about 30°. This illustrates the focus capability of the nodding pattern. Note that in the right of Fig.12, the distance to the satellite mockup is smaller compared to the nodding configuration. This is due to the different mounting orientations of the Sensor Head for nodding and centric configuration (compare Fig.4) while the distance of the robots was the same for both tests.

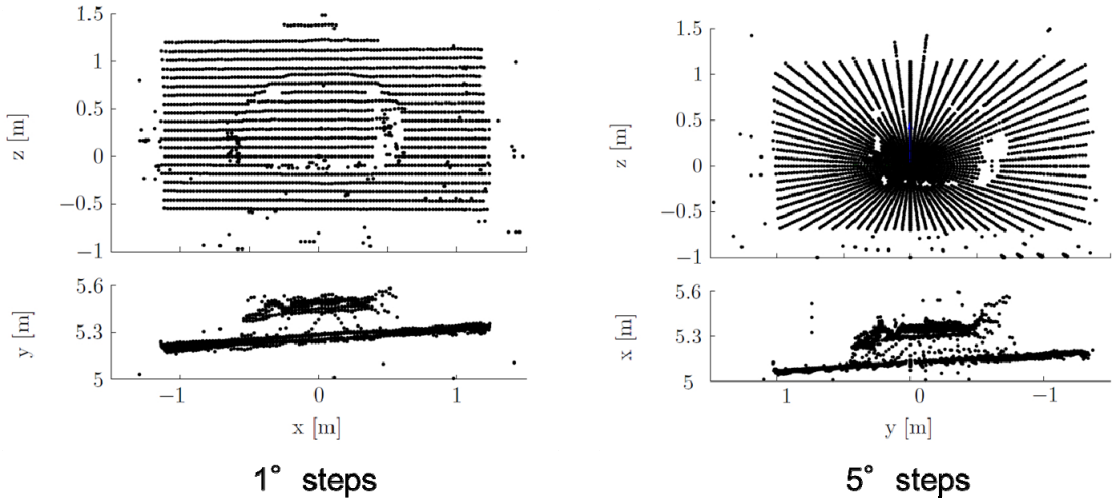

Fig. 12: *Point clouds of preliminary tests at EPOS. Focused and magnified so that the target object can be seen distinctly.*

In order to get an idea about the influence of illumination, we estimated the standard deviation of a representative point on the target mockup by sampling this point 1000 times, at a mean distance of 5.128 m. In Fig.13 the standard deviation is given for darkness, a 2.5 kW and 5 kW conventional spotlight as well as for the 12 kW daylight spotlight which provides a sun-like power density on the satellite mockup. In the latter case, we obtain a standard deviation of about 14 mm or a 3σ of 42 mm. Apparently, the rangefinder of the UTM-30LX shows increasing noise as a reaction to increasing illumination power density on the satellite mockup. However, we consider even the worst case standard deviation of 14 mm to be a reasonable value.

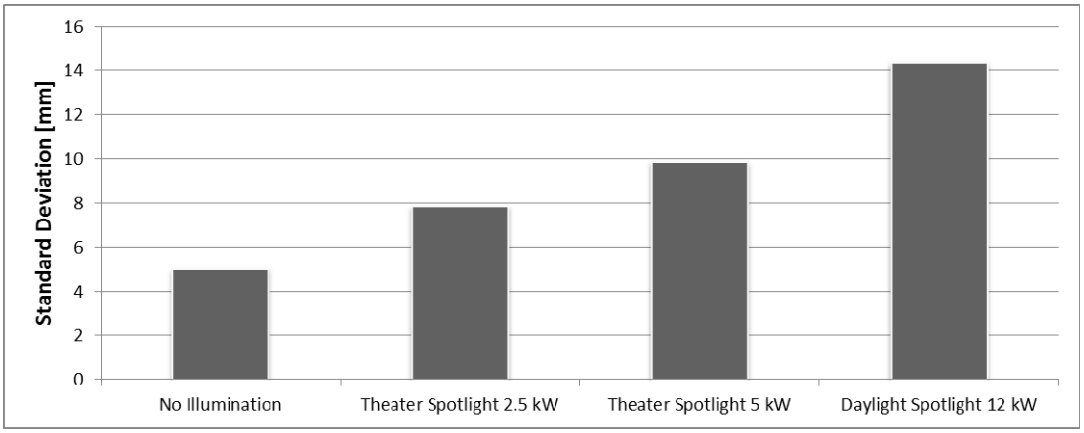

Fig. 13: *Standard deviation of range measurement depending on illumination. Mean distance is 5.128 m.*

The angular accuracy of the sensor cannot be given at this point, since calibration was not possible yet. However, we make a rough estimate based on theoretical values. According to the manufacturer (statements made via e-mail), the UTM-30LX' angular displacement jitter is less than 0.1 %, i. e. 0.00025° considering the resolution of 0.25°. For axis B, we expect the accuracy to be dominantly influenced by the encoder's accuracy of ±0.03°.

In summary, the sensor can be expected to meet the performance requirements of 50 mm range accuracy and 0.1° angular accuracy, as formulated in Sec.1.

5. CONCLUSION

In the On-Orbit Servicing & Autonomy group at the German Space Operations Center (GSOC), a COTS based 3D scanning LiDAR is developed. Primarily, it shall serve as a sensor for research and development of GNC algorithms for autonomous spacecraft relative navigation as well as for Hardware in the Loop simulations at the European Proximity Operations Simulator. Also, it will be used as a research platform for developing novel

concepts and software for LiDAR based autonomous Rendezvous and Docking. The sensor uses a 2D laser rangefinder that is extended by an additional rotary axis. Two principally different scanning patterns can be realized: a periodically nodding pattern resulting in a raster-like point distribution and a continuously rolling centric pattern resulting in a especially large point density in the Region of Interest. A real-time sensor control and processing system is currently being implemented. It uses an embedded system with a strongly coupled combination of an FPGA and a CPU, thereby combining the advantages of both technologies. It not only controls the sensor but processes the point cloud data to optain the complete pose of the target object. Preliminary manual tests of the Sensor Head were conducted at EPOS. Although no software calibration was done at this stage of development, the obtained point clouds can be considered to be of reasonable quality. With target object illumination comparable to those at Earth orbit around the sun (power density and spectrum), the range's standard deviation of a representative range measurement was about 14 mm. From a rough theoretical estimate, the overall angular accuracy of the sensor is expected to be about 0.03°.

REFERENCES

[1] A. Ellery, J. Kreisel, B. Sommer, "The case for robotic on-orbit servicing of spacecraft: Spacecraft reliability is a myth", *Acta Astronautica*, vol. 63, pp. 632-648, 2008.

[2] E. Stoll, J. Letschnik, U. Walter, J. Artigas, P. Kremer, C.Preusche, G. Hirzinger, „On-orbit servicing", *IEEE Robotics & Automation Magazine*, vol. 16, pp. 29-30, 2009.

[3] H. Benninghoff, T. Boge, F. Rems, "Autonomous Navigation for On-Orbit Servicing", *KI – Künstliche Intelligenz*, 2014, doi: 10.1007/s13218-014-0297-0

[4] S.-I. Nishida, S. Kawamoto, Y. Okawa, F. Terui, S. Kitamura, "Space debris removal using a small satellite", *Acta Astronautica*, vol. 65, pp. 95-102, 2009.

[5] C. Bonnal, J.-M. Ruault, M.-C. Desjean, "Active debris removal: Recent progress and current trends", *Acta Astronautica*, vol. 85, pp. 51-60, 2013.

[6] M. Nimelman, J. Tripp, G. Bailak, J. Bolger, "Spaceborne scanning lidar system (SSLS) upgrade path", *Proceedings of SPIE*, vol. 6201, 2006.

[7] B. Moebius, A. Ullrich, „Tele-Goniometer Rendezvous Sensor – an Existing Sensor and its Growth Potential", *Proceedings of the 24th International Symposium on Space Technology and Science*, 2004, Miyazaki, Japan.

[8] S. Ruel, T. Luu, A. Berube, „Space Shuttle Testing of the TriDAR 3D Rendezvous and Docking Sensor", *Journal of Field Robotics*, vol. 29, pp. 535-553, 2012.

[9] H. Benninghoff, T. Boge, T. Tzschichholz, „Hardware-in-the-Loop Rendezvous Simulation Involving an Autonomous Guidance, Navigation and Control System", *1st IAA Conference on Dynamics and Control of Space Systems*, 19-21 March, 2012, Porto, Portugal.

[10] O. Ma, A. Flores-Abad, T. Boge, "Use of industrial robots for hardware-in-the-loop simulation of satellite rendezvous and docking", *Acta Astronautica*, vol. 81, pp. 335-347, 2012.

[11] T. Boge, H. Benninghoff, T. Tzschichholz, „Hardware-in-the-loop Rendezvous Simulation using Vision Based Sensor", *8th International ESA Conference on Guidance, Navigation & Control Systems*, 5.-10. June, 2010, Karlsbad, Tschechien.

[12] T. Tzschichholz, T. Boge, H. Benninghoff, „A Flexible Image Processing Framework for Vision-based Navigation Using Monocular Image Sensors", *8th International ESA Conference on Guidance, Navigation & Control Systems*, 5.-10. June, 2010, Karlsbad, Tschechien.

[13] T. Tzschichholz, L. Ma, K. Schilling, „Model-based spacecraft pose estimation and motion prediction using a photonic mixer device camera", *Acta Astronautica*, vol. 68, pp. 1156-1167, 2011.

[14] Hokuyo Automatic Co. Ltd, „Scanning Laser Range Finder UTM-30LX/LN Specification", 2009.5.18, http://de.manu-systems.com/UTM-30LX_spec.pdf, 17.04.2014.

[15] A. Desai, D. Huber, „Objective Evaluation of Scanning Ladar Configurations for Mobile Robots", *IEEE/RSJ International Conference on Intelligent Robots and Systems*, 2009, St. Louis, MO, United States.

[16] LTN Servotechnik GmbH, "Slip-Ring SC020 Datasheet", http://www.ltn.de/uploads/tx_news/SC020_EN_01.pdf, October 2013.

[17] Sick AG, "AFS60/AFM60 Product Info", www.sick.com, 8012884/2012-06-19

[18] Harmonic Drive AG, "Product Description CobraDrive", www.harmonicdrive.de.

[19] Altera, "Cyclone V SoC Development Board Reference Manual", www.altera.com, November 2013